

Isotope and density profile effects on pedestal neoclassical transport

S. Buller^{1, a)} and I. Pusztai¹

Department of Physics, Chalmers University of Technology, SE-41296 Göteborg, Sweden

(Dated: 24 July 2021)

Cross-field neoclassical transport of heat, particles and momentum is studied in sharp density pedestals, with a focus on isotope and profile effects, using a radially global approach. Global effects – which tend to reduce the peak ion heat flux, and shift it outward – increase with isotope mass for fixed profiles. The heat flux reduction exhibits a saturation with a favorable isotopic trend. A significant part of the heat flux can be convective even in pure plasmas, unlike in the plasma core, and it is sensitive to how momentum sources are distributed between the various species. In particular, if only ion momentum sources are allowed, in global simulations of pure plasmas the ion particle flux remains close to its local value, while this may not be the case for simulations with isotope mixtures or electron momentum sources. The radial angular momentum transport that is a finite orbit width effect, is found to be strongly correlated with heat sources.

Keywords: neoclassical transport, tokamak, radially global, pedestal, isotope effect

I. INTRODUCTION

The magnetic fusion community acquired its vast operational experience and experimental knowledge of stability and confinement predominantly from deuterium (D) – and to some extent hydrogen (H) – discharges. There is much less experience with the reactor relevant deuterium-tritium mixture (DT), which has only been used in a limited number of discharges in JET¹ and TFTR². Likewise, ITER³ will first operate with He and H⁴, and then with D, before starting its DT operation. To be confident in our predictions for reactor-scale devices, such as ITER, we therefore need to understand how various physical processes are affected by changes in the isotope composition of the bulk plasma.

In particular, the *isotope scaling* of the energy confinement has been a long-standing unresolved issue in the field^{5–14}. The confinement in the plasma core is observed to be broadly consistent with turbulent transport predictions of gyrokinetic codes, see Ref. 15 and references therein. Multiscale gyrokinetics – the theoretical foundation of these codes – assumes characteristic fluctuation time and length scales that correspond to gyro-Bohm level fluxes. Naïve applications of the gyro-Bohm scaling predict an increased transport with increasing isotope mass. In contrast, the global energy confinement is experimentally observed to improve with increasing isotope mass^{16–19}.

The exact strength of this favorable isotope scaling varies greatly between different operational regimes. As general trends, in Ohmic and L-mode plasmas the isotope scaling of confinement is weak, while H-mode D plasmas show a consistently higher confinement time than H plasmas^{18,20,21}. Since the H-mode features an edge transport barrier – commonly referred to as the *pedestal* – such differences between operational regimes suggest that different mechanisms may be responsible for the isotope scaling in the core and in the pedestal²²; the latter being the focus of this work.

In the pedestal, the plasma parameters can vary significantly over a thermal orbit width, so that the transport at a given minor radius no longer can be characterized by local profile

^{a)}Electronic mail: bstefan@chalmers.se

values, but depends on values at nearby radii. Such transport is said to be *radially global*, and simple dimensionally motivated or diffusive scaling estimates, such as gyro-Bohm, may not be appropriate. The distance over which the perturbed distribution function is radially coupled scales with the thermal ion orbit width, which introduces a mass dependence. In this paper we consider the impact of the radial coupling on neoclassical heat, particle and momentum fluxes, particularly in relation to isotope effects and characteristic pedestal features, such as pedestal height and width.

Specifically, we study how characteristic features of pedestal density profiles affect the radially global transport fluxes, by varying pedestal properties of model profiles in simulations with different isotopes. A self-consistent modeling of how the profiles themselves are affected by changes in isotopic composition – due to e.g. atomic physics processes^{23,24}, magnetohydrodynamic stability²⁵ and other processes – is beyond the scope of this study.

We solve a global δf drift kinetic equation numerically using the PERFECT^{26,27} solver. This tool represents an intermediate step between the conventionally employed, core-relevant local δf codes^{28,29}, and the generally valid, but computationally challenging full- f approach³⁰. PERFECT allows density and potential profiles that vary on ion orbit-width scales, while the linearization around a Maxwell-Boltzmann distribution requires that the ion temperature varies weakly over an ion orbit width and that the ion diamagnetic and $E \times B$ flows nearly cancel in the large gradient region – a situation referred to as *electrostatic ion confinement*, which has been borne out in experimental results^{31,32}.

The remainder of this paper is structured as follows: In Sec. II we discuss the details of our modeling, starting by explaining relevant aspects of the global δf model. We then discuss the choices made in setting up our model profiles, and finally provide technical details on the magnetic geometry and normalization. The presentation and interpretation of simulation results is done in Sec. III. In Sec. III A, we consider isotope mass effects on the ion heat flux using a fixed set of baseline profiles, showing increasing global effects with isotope mass due to an increasing orbit width. We then consider the impact of changes in the pedestal density profile in Sec. III B. We quantify the importance of global effects on the ion heat flux by two parameters and study their behavior in terms of profile features and bulk isotopes in Sec. III C. We find that the peak ion heat flux is mostly reduced and it is shifted outwards by global effects, with a larger possible reduction for heavier isotopes. Finally, we discuss species and profile effects on particle and angular momentum transport in Sec. III D, and correlate momentum transport with heat sources. Our results are then summarized in Sec. IV.

II. MODELING CHOICES

A. Model

We solve the following global δf drift kinetic equation²⁷

$$(v_{\parallel} \mathbf{b} + \mathbf{v}_d) \cdot \nabla g - C_l[g] = -\mathbf{v}_m \cdot \nabla f_M + S, \quad (1)$$

where $g = f - f_M + (Ze\Phi_1/T)f_M$ is the non-adiabatic perturbed distribution, f is the gyroaveraged distribution function, $f_M = [m/(2\pi T)]^{3/2} \eta e^{-W/T}$ is a Maxwellian, $W = mv^2/2 + Ze\Phi$ is the unperturbed total energy, m and Ze are the charge and the mass of the species, with e the elementary charge, $\eta = ne^{Ze\Phi/T}$ is the pseudo-density, n and T are the density and the temperature of the species, and $\Phi + \Phi_1$ is the total electrostatic potential with a small perturbed component Φ_1 defined such as to vanish on flux surface average. The flux surface average density and pressure of the species are all contained in f_M . In other words, any poloidal variations in plasma parameters are treated as perturbations. Furthermore, $v_{\parallel} = \mathbf{v} \cdot \mathbf{b}$, with \mathbf{v} the velocity, $\mathbf{b} \equiv \mathbf{B}/B$, with \mathbf{B} the magnetic field and $B \equiv |\mathbf{B}|$; $\mathbf{v}_d = \mathbf{v}_E + \mathbf{v}_m$ is the unperturbed drift velocity, $\mathbf{v}_m = v_{\parallel}^2 \Omega^{-1} \nabla \times \mathbf{b} + v_{\perp}^2 (2\Omega B^2)^{-1} \mathbf{B} \times \nabla B$ is the magnetic drift velocity, $\mathbf{v}_E = B^{-2} \mathbf{B} \times \nabla \Phi_0$ is the $E \times B$ drift velocity; $\Omega = ZeB/m$ is the gyrofrequency, and $\mathbf{v}_{\perp} = \mathbf{v} - v_{\parallel} \mathbf{b}$ is the velocity perpendicular to \mathbf{b} . C denotes the

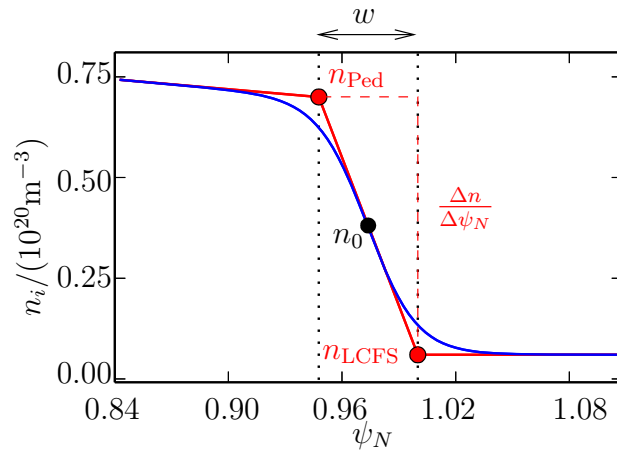


FIG. 1: The baseline density profile used in this work, with profile parameters highlighted.

linearized Fokker-Planck collision operator. The gradients are taken holding W and the magnetic moment, $\mu = mv_{\perp}^2/(2B)$, constant. S is a source term, which accounts for both real sources (e.g. ionization, radiative energy loss) and possible divergence in the fluxes other than those captured by our solution g (e.g. a radially varying turbulent particle flux). We have omitted species indices to streamline the notation; in cases where this leads to ambiguity, a lower index a will be used.

Equation (1) is an approximation of the drift-kinetic equation only when the distribution function is close to a flux-surface Maxwell-Boltzmann distribution: $f/f_M - 1 \ll 1$. This requires that the temperature T and pseudo-density η associated with the Maxwellian do not vary significantly over a thermal orbit width, while the density n can vary sharply – provided that the electrostatic potential Φ is such that η is slowly varying. In practice these restrictions are only a concern for the various ion species; thus, to avoid large deviations from Maxwellian ion distributions, we consider ion profiles without ion temperature pedestals. As T_e and η_e need only to be slowly varying on an electron orbit width scale, they are allowed to be comparably sharp to $n_e \sim n_i$ (e and i subscripts refer to electrons and bulk ions). For more details on the self-consistent ordering considered here the reader is referred to Ref. 27,33.

B. Input profiles

As we have seen in the previous section, even though there are restrictions on the T and η profiles we are free to choose an arbitrary density profile, which allows us to study the effects of different density pedestals. For this purpose, we use model density profiles based on the *mtanh profile*^{34,35} which is often used to represent the radial profile dependence of the pedestal. The mtanh profile defines three regions: a *core* region, where the density varies over length scales comparable to the minor radius of the device; a *pedestal* region, where this variation is comparable to a typical thermal ion orbit width; and a *SOL* (Scrape-Off Layer) region with very small gradients (to be discussed further in relation to boundary conditions at the end of Sec. IIB); see Fig. 1.

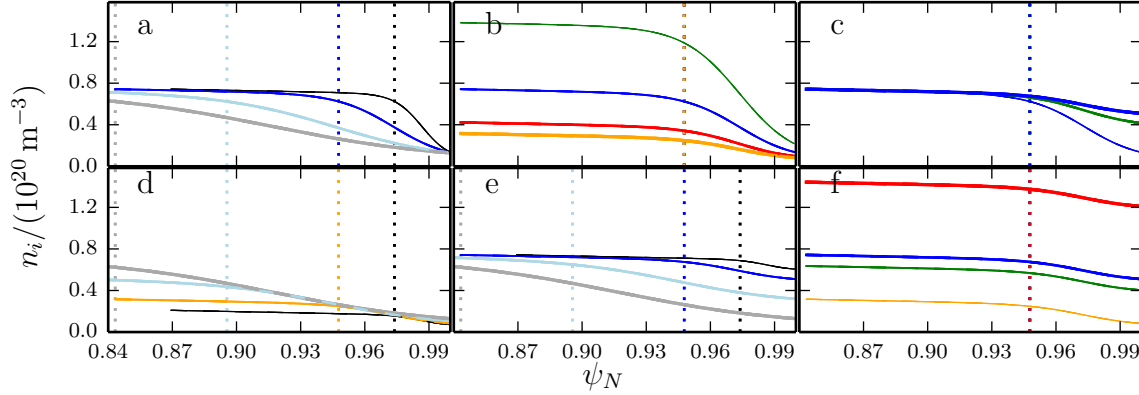


FIG. 2: Input profiles of n_i in the various scans: (a) $\frac{\Delta n}{\Delta \psi_N}$ - w , (b) $\frac{\Delta n}{\Delta \psi_N}$ -Ped, (c) $\frac{\Delta n}{\Delta \psi_N}$ -LCFS, (d) w -Ped, (e) w -LCFS, (f) Ped-LCFS. Thinner lines correspond to sharper or narrower pedestals in the scan.

Specifically, a generic mtanh plasma profile X is given by

$$\begin{aligned}
 X = & \frac{1}{2} \left[X_{\text{ped}} + X_{\text{SOL}} + \frac{w}{2} \left\{ \left. \frac{dX}{d\psi_N} \right|_{\text{core}} - \left. \frac{dX}{d\psi_N} \right|_{\text{SOL}} \right\} \right] \\
 & + \frac{\tanh(x)}{2} \left[X_{\text{SOL}} - X_{\text{ped}} - \frac{w}{2} \left\{ \left. \frac{dX}{d\psi_N} \right|_{\text{core}} + \left. \frac{dX}{d\psi_N} \right|_{\text{SOL}} \right\} \right] \\
 & + \frac{\left. \frac{dX}{d\psi_N} \right|_{\text{core}} (\psi_{N0} - \psi_0) e^{-x} + \left. \frac{dX}{d\psi_N} \right|_{\text{SOL}} (\psi_N - \psi_{N0}) e^x}{e^{-x} + e^x},
 \end{aligned} \tag{2}$$

where $x = \frac{(\psi_N - \psi_{N0})}{w/2}$ is a radial coordinate, with $\psi_N = \psi/\psi_{\text{LCFS}}$ being the normalized poloidal flux, $2\pi\psi$ the poloidal magnetic flux (satisfying $|\nabla\psi| = RB_P$, with R the major radius and B_P the poloidal magnetic field), ψ_{LCFS} is the value of ψ at the last closed flux surface (LCFS), ψ_{N0} the ψ_N -point in the middle of the pedestal and w characterizes the pedestal width. Parameters X_{ped} and X_{LCFS} represent the values of the the asymptotic, linear core and SOL profiles extrapolated to the pedestal top and the LCFS locations, respectively (marked with red circles in Fig. 1), while $\left. \frac{dX}{d\psi_N} \right|_{\text{core}}$ and $\left. \frac{dX}{d\psi_N} \right|_{\text{SOL}}$ are the asymptotic core and SOL gradients.

In this work, we categorize our density pedestals in terms of four parameters of common interest: n_{ped} , n_{LCFS} ; the width in ψ_N , w ; and the density gradient in the middle of the pedestal, $\frac{\Delta n}{\Delta \psi_N}$. The former three quantities appear directly in (2), while the latter is defined by the relation

$$n_{\text{ped}} + \left(\frac{\Delta n}{\Delta \psi_N} \right) w - n_{\text{LCFS}} = 0; \tag{3}$$

see also Fig. 1 for a visual definition of the four pedestal parameters.

We wish to investigate the dependence of transport on these pedestal parameters. As the parameters are all related through (3), we vary two of these parameters at a time, while keeping the two remaining parameters fixed. This yields 6 different scans.

For our baseline density pedestal, we use the pedestal parameters $\hat{n}_{\text{ped}} = 0.7$, $w = 0.0522$, $\frac{\Delta \hat{n}}{\Delta \psi_N} = -12.3$ and $\hat{n}_{\text{LCFS}} = 0.06$; these values are comparable to those of the ASDEX Upgrade pedestal shown in Fig. 1 of Ref. 36. Here, \hat{n} refers to the density n given in 10^{20} m^{-3} . Subsequent density profiles were obtained by scaling two of the pedestal parameters about the baseline value. The pedestal parameters for all scans are displayed in Tab. I, with the scanned values written in bold letters. From these parameters, we

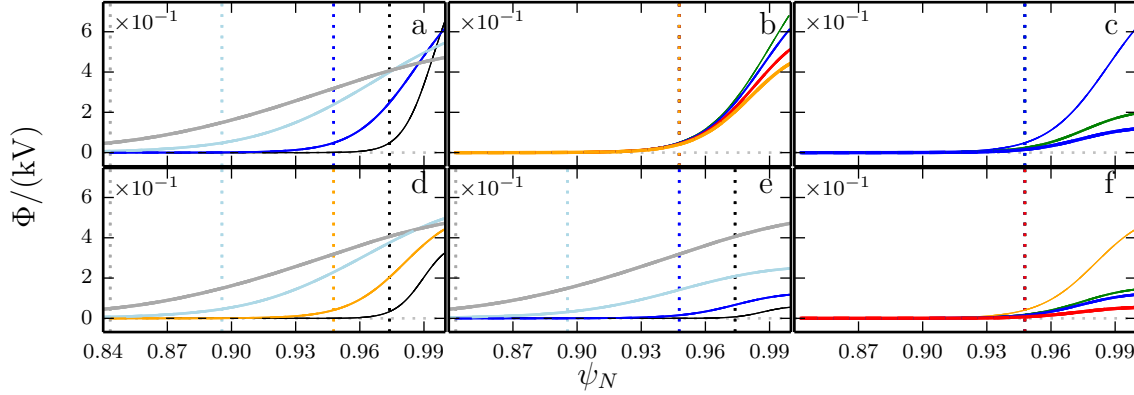


FIG. 3: Electrostatic potentials Φ corresponding to the n_i profiles in Fig. 2. Thinner lines correspond to sharper or narrower pedestals in the scan.

TABLE I: Pedestal parameters corresponding to density profiles in Fig. 2. The scanned parameters are written with boldface letters.

w	$\frac{\Delta n}{\Delta \psi_N}$	n_{Ped}	n_{LCFS}
0.0261	-24.5	0.7	0.06
0.0522	-12.3	0.7	0.06
0.104	-6.13	0.7	0.06
0.157	-4.08	0.7	0.06
0.0522	-24.5	1.34	0.06
0.0522	-12.3	0.7	0.06
0.0522	-6.13	0.38	0.06
0.0522	-4.08	0.273	0.06
0.0522	-12.3	0.7	0.06
0.0522	-6.13	0.7	0.38
0.0522	-4.08	0.7	0.487
0.0261	-4.08	0.167	0.06
0.0522	-4.08	0.273	0.06
0.104	-4.08	0.487	0.06
0.157	-4.08	0.7	0.06
0.0261	-4.08	0.7	0.593
0.0522	-4.08	0.7	0.487
0.104	-4.08	0.7	0.273
0.157	-4.08	0.7	0.06
0.0522	-4.08	0.273	0.06
0.0522	-4.08	0.593	0.38
0.0522	-4.08	0.7	0.487
0.0522	-4.08	1.4	1.19

construct mtanh density profiles, shown in Fig. 2, where the different sub-figures correspond to the various scans. These profiles all have the same asymptotic core density gradient $\left. \frac{\partial \hat{n}}{\partial \psi_N} \right|_{\text{core}} = -0.40616$ (again, similar to the corresponding value in Fig. 1 of Ref. 36), and $\left. \frac{\partial \hat{n}}{\partial \psi_N} \right|_{\text{SOL}}$ is fixed at zero.

As we cannot have a pedestal in the ion temperature profile, T_i is kept fixed at core-like gradients during the scan, as shown in Fig. 4. The profile features a transition in ∇T_i centered around the pedestal top ($\psi_N \approx 0.96$ in Fig. 4), as this feature is important for the qualitative behavior of both in-flux-surface and cross-field fluxes³³, and mimics the change in gradients at the top of a real pedestal. The asymptotic gradients are $\left. \frac{\partial \hat{T}_i}{\partial \psi_N} \right|_{\text{core}} = -0.5$

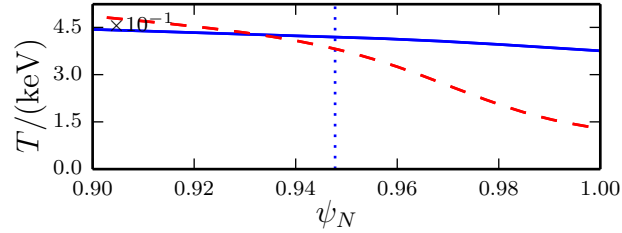


FIG. 4: The baseline T_i (solid) and T_e (dashed) profiles.

and $\left. \frac{\partial \hat{T}_i}{\partial \psi_N} \right|_{\text{SOL}} = -0.9$, and $\hat{T}_{i,\text{Ped}} = 0.42$, where \hat{T} denotes temperature in units of 1 keV.

The baseline electron temperature profile, T_e , is an mtanh profile with the following parameters: $w = 0.0522$, $\frac{\Delta \hat{T}_e}{\Delta \psi_N} = -6.12$, $\hat{T}_{e,\text{Ped}} = 0.42$, and $\hat{T}_{e,\text{LCFS}} = 0.1$. In the scans, we change the T_e pedestal width to match that of n_i in each case, while $T_{e,\text{Ped}}$ and $T_{e,\text{LCFS}}$ are kept fixed. Similarly, the transition in ∇T_i is moved to match the location of the pedestal top, and its width is scaled when the pedestal width is varied. The T_i profile is otherwise kept fixed. The baseline T_e and T_i profiles are shown in Fig. 4.

The potential, Φ , is chosen to yield a slowly varying η_i : specifically, η_i is taken to be an mtanh profile asymptotically equal to the n_i profile in the core, and with core and pedestal gradients equal to the n_i core gradients – the resulting potentials are shown in Fig. 3. Although there is some arbitrariness in choosing Φ this way, it yields an electric field balancing the ion pedestal pressure gradient – consistent with typical experimental observations^{31,32,37}.

Although the above profiles have a SOL region, the PERFECT code assumes closed field line topology. Rather than a physical SOL, these regions should be thought of as a numerical buffer zone, such that the radial boundary conditions we impose on the global drift-kinetic equation do not affect the results in the pedestal. Accordingly we do not show results in this region, because they are not physically meaningful. In this region we set the gradients to be low, so that the local solution can be used as a boundary condition at both radial boundaries where particle trajectories enter the domain.

C. Magnetic geometry

For the magnetic geometry, we use a model Miller equilibrium³⁸ with the radially constant parameters: $\kappa = 1.58$, $\delta = 0.24$, $s_\delta = 0.845$, $s_\kappa = 0.479$, $dR/dr = -0.14$, $q = 3.5$. Here, κ is the elongation, δ is the triangularity, and s_κ and s_δ quantify the radial variation of these parameters; R is the major radius, r the minor radius and q the safety factor.

The radially uniform magnetic geometry, together with the weakly varying ion temperature profiles, means that the thermal ion orbit-width is approximately constant throughout the pedestal. Thus, the radial coupling length of a given species is close to constant in the simulation domain, providing a simple setting to investigate global effects. In reality, magnetic geometry parameters can change significantly across the pedestal, which would both change the magnitude and correlation length of the neoclassical transport in the vicinity of the separatrix. However, our results should be qualitatively correct in more complicated geometries, as long as the radial coupling length continues to scale with isotope mass.

In scans affecting the pedestal width we keep the LCFS location fixed and move only the pedestal top location.

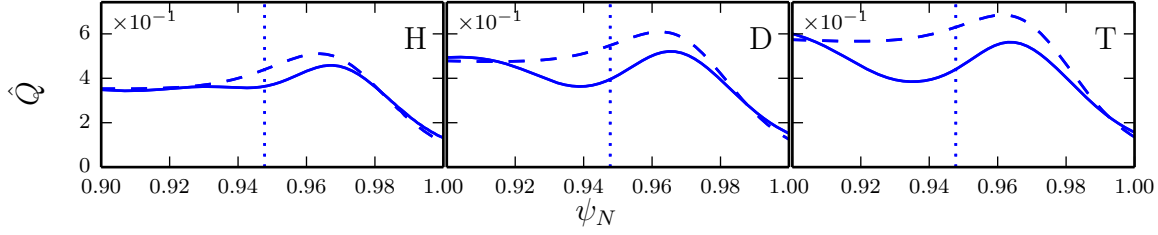


FIG. 5: Normalized ion heat flux \hat{Q}_i for the baseline profile (blue in Fig. 2) in H, D and T plasmas. Solid (dashed) curves are from global (local) simulations.

D. Normalization of simulation outputs

Quantities with a hat are normalized to a reference quantity, $\hat{X} = X/\bar{X}$. The reference quantities used in this work are $\bar{R} = 1.51$ m, $\bar{B} = 3.00$ T, $\bar{n} = 10^{20}$ m $^{-3}$, $\bar{T} = e\Phi = 1$ keV, $\bar{m} = m_{\text{D}}$, where m_{D} is the mass of deuterium. From these, we define a reference speed as $\bar{v} = \sqrt{2\bar{T}/\bar{m}}$, and the dimensionless constant $\Delta = \bar{m}\bar{v}/(e\bar{B}\bar{R}) \ll 1$, which is representative of the normalized gyroradius. Specific normalizations are as follows: particle flux, $\hat{\Gamma}_a = \int d^3v g_a \mathbf{v}_{ma}/(\bar{n}\bar{v})$; radial flux of co-current toroidal angular momentum (divided by mass), $\hat{\Pi}_a = \int d^3v g_a v_{\parallel} I \mathbf{v}_{ma}/(\bar{n}\bar{v}^2 \bar{R}B)$, with $I(\psi) = RB_{\text{T}}$ and B_{T} the toroidal magnetic field; heat flux, $\hat{Q}_a = \int d^3v g_a m_a v^2 \mathbf{v}_{ma}/(2\bar{T}\bar{n}\bar{v})$, that is related to the conductive heat flux by $\hat{q}_a = \hat{Q}_a - (5/2)\hat{T}\hat{\Gamma}_a$; and sources $\hat{S}_a = \bar{v}^2 \bar{R}S_a/(\Delta\bar{n}\hat{m}_a^{3/2})$. In addition, we define the normalized scalar radial particle flux

$$\hat{\Gamma}_a = \frac{\hat{V}'}{\Delta^2 \pi \bar{R} \bar{B}} \langle \hat{\Gamma}_a \cdot \nabla \psi \rangle, \quad (4)$$

and analogously the scalar heat and angular momentum fluxes, where we introduced the normalized incremental volume $\hat{V}' = (\bar{B}/\bar{R})d\psi V$, with $V(\psi)$ the volume within the flux surface ψ , and the flux surface average is denoted by $\langle \cdot \rangle$.

III. SIMULATION RESULTS

A. Species effects on ion energy flux

In an experiment, changing the bulk ion species causes modifications to all plasma parameter profiles across the radius. Furthermore, different quantities can be kept fixed in a species scan (e.g. total heating power, average density, etc.), while others change. Here, we intend to isolate the direct effect of the species from such indirect effects. Thus we keep all plasma parameter profiles fixed, as specified in the previous section (line 2 in Tab. I), and perform both radially local and global simulations with various hydrogen isotopes: protium (H, which we will simply refer to as hydrogen), deuterium (D) and tritium (T). Out of these, tritium has the largest orbit width, and is hence expected to show the largest differences between the local and global models for a fixed pedestal.

The resulting ion heat fluxes Q_i for the different isotopes are displayed in the panels of Fig. 5, where the solid (dashed) curves correspond to global (local) results, and vertical lines indicate the nominal location of the pedestal top. As expected, the deviation between local and global results is the weakest in the H simulation. This is apparent in two ways: global effects persist for a shorter distance into the near-pedestal core – owing to the shorter radial coupling length that scales with orbit width – and the difference at a given radius is typically smaller than for the heavier isotopes. In particular the global *pedestal peak-value* (PPV), which is the global maximum value inside the pedestal, is closer to the local peak

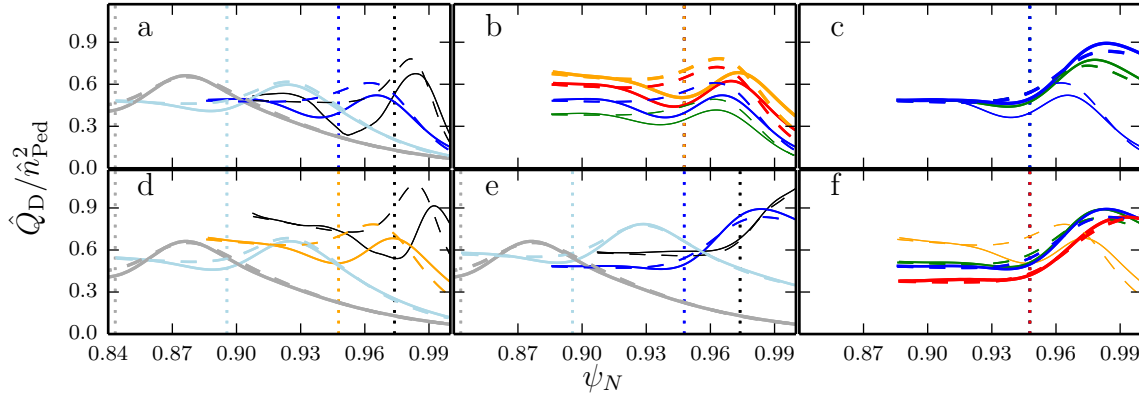


FIG. 6: Deuterium heat flux normalized as $\hat{Q}_D/\hat{n}_{\text{Ped}}^2$ from deuterium simulations using the profiles in Fig. 2. Solid (dashed) curves are from global (local) simulations. Thinner lines correspond to sharper or narrower pedestals in the scan.

value. (The PPV will be used later to characterize differences in scans.) In comparison, for the heavier isotopes, the global PPV is further reduced compared to the local one, and global effects persist further into the core.

The deviation between local and global results is not a monotonic function of the local gradient, rather it appears as a strongly damped oscillation that dies away as we move further into the core. In this example it happens to lead to a local minimum in the global Q_i in the near-pedestal core, for instance, as observed around $\psi_N = 0.94$ for Q_D in Fig. 5. Estimating the coupling-length r_i as the distance from the pedestal top where the global and local values intersect for the first time, we get $r_H = 0.022$, $r_D = 0.033$, and $r_T = 0.042$, which appears to have a mass-scaling $r \propto m^{0.56}$, which appears consistent with thermal orbit width scaling, $r \propto m^{1/2}$. Interestingly, the global Q_i inside the pedestal is rather similar between the three isotopes, even though the local flux increases due to $\nu_{ii}\rho_i^2 \propto m^{1/2}$ (this random walk estimate of diffusive transport includes the ion self-collision frequency ν_{ii} , and the thermal ion Larmor radius ρ_i).

B. Varying pedestal profiles

Next, we consider the qualitative changes in the ion heat flux \hat{Q}_i when the pedestal profiles are modified as in the scans shown in Fig. 2. Here we will keep the isotope fixed. The deuterium heat flux \hat{Q}_D calculated for the different input profiles of Fig. 2 is shown in Fig. 6, where again, local simulations are indicated by dashed lines. The dimensionless heat flux \hat{Q} is divided by \hat{n}_{Ped}^2 , to compensate for its expected density scaling in the banana regime, and so assist the comparison of the results.

In Fig. 6a, corresponding to an increasing pedestal width at fixed pedestal top density, we see how the fluxes become increasingly more local as the pedestal gets wider and the pedestal gradient decreases. The result for the narrowest profile (black) yields significant global effects in the near-pedestal core (with a minimum at around $\psi_N = 0.95$), although the absolute effect on the PPV is not larger than for the baseline profile result (blue).

Fig. 6b corresponds to a pedestal height scan for fixed pedestal width, producing the same representative pedestal gradients as those in the Fig. 6a scan. One crucial difference is that while the maximum electric field in the pedestal decreased significantly as the pedestal width increased, it remains less affected in this scan (compare the slopes in Fig. 3a and b), as here $\partial_\psi \ln n$ does not change strongly, except near the LCFS, since n_{LCFS} is kept fixed. As the Fig. 2b profiles are more similar to each other in this sense, we see less pronounced variation in the difference between local and global fluxes. If anything, the difference is

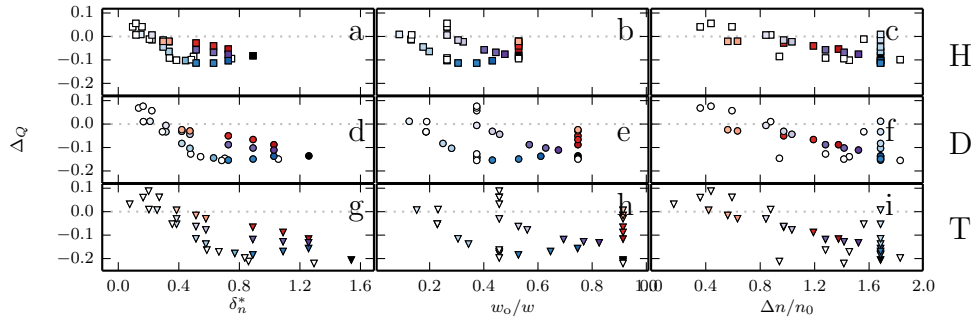


FIG. 7: Relative deviation between global and local peak heat flux values in the pedestal. Ion species is H (a-c), D (d-f), T (g-i). Representative values of (a,d,g) ratio of orbit width and density scale length, (b,e,h) ratio of orbit width and pedestal width, (c,f,i) ratio of the density drop across the pedestal and the average pedestal density.

somewhat larger in the cases with lower pedestal top density, curiously. This may be a consequence of keeping the ion temperature fixed in this scan: when the global effects due to the n are reduced, global effects due to T_i may become increasingly important, and these are perhaps not captured in the n_{Ped} normalization.

In the case shown in Fig. 6c the pedestal width and pedestal top density are kept fixed, while the n_{LCFS} is modified leading to a variation in density gradient. The resulting density gradients are the same as for the baseline profile and the reduced gradient cases in Fig. 2a, with the largest gradient pedestal displaying the largest global effects. As the n_{LCFS} increases, the maximum of the fluxes – both local and global – is shifted outward.

In Fig. 6d-e, we study the influence of pedestal width using profiles with maximum gradients similar to that in the widest pedestal of Fig. 2a. In Fig. 6d we show simulations with fixed n_{LCFS} , which implies that n_{Ped} increases with w . While the wide pedestal cases are rather close to local behavior, the thin pedestal results become surprisingly strongly non-local. This may partly be due to the large electric field in that case (compare the slopes in Fig. 3d), and the fact that $\partial_\psi \ln n$ reaches higher values in the small pedestal (as $\partial_\psi \ln n$ is largest in the middle of our model pedestals). Finally, it could also be related to more abrupt radial changes in the profile that give rise to strong sources.

However, the latter cause alone is not sufficient to generate large deviations from the local behavior, as seen from the results keeping the pedestal top density fixed in Fig. 6e. In this scan the deviations between local and global results are comparable for all n_{LCFS} values, despite the larger (but still small) logarithmic gradient for the narrower profile. This similarity could be a result of the similar electric fields in these cases (consider the slopes in Fig. 3e).

In the last scan, shown in Fig. 6f, we keep the pedestal width and the gradient fixed, but shift n_{LCFS} and n_{Ped} simultaneously. The case with the lowest density – that has the most realistic pedestal shape – has the highest $\partial_\psi \ln n$ and the strongest radial electric field and, as expected, it exhibits the strongest deviation between the local and global results. As the density is increased we observe the location of the maximum flux to shift outward in both the local and the global results. This shift is caused by the lower relative drop in density across the pedestal in the higher density cases, noting that the local flux depends on the local density instead of n_{Ped} .

C. Peak heat flux and its location for various pedestals and isotopes

As we have seen in Sec. IIIB, the changes in heat flux profiles in response to changes in pedestal parameters are rather complex; in particular the strength of global effects may not follow intuitively expected trends. To quantify the profile and isotope effects identified in the

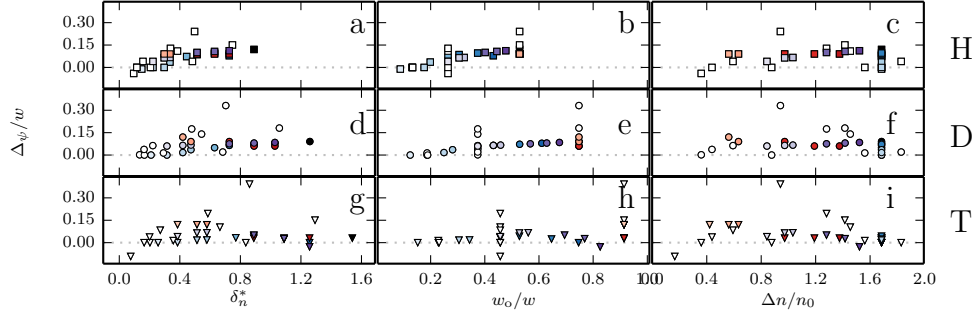


FIG. 8: Relative deviation between global and local peak heat flux locations in the pedestal relative to the pedestal width. Ion species is H (a-c), D (d-f), T (g-i). Representative values of (a,d,g) ratio of orbit width and density scale length, (b,e,h) ratio of orbit width and pedestal width, (c,f,i) ratio of the density drop across the pedestal and the average pedestal density.

previous sections, we extract the Pedestal Peak Values (PPVs) of Q_i and the ψ_N location of these peaks. The significance of the PPV heat flux lies in the fact that it represents a lower bound on the total heat flux, and that in some experiments the total ion energy flux is close to neoclassical predictions³⁹. Since we are mainly interested in deviations from the local theory, we define $\Delta_{GL}X = X_G - X_L$: the difference in parameter X between a global and a corresponding local simulation. Fig. 7, shows the relative difference between local and global ion heat flux PPVs $\Delta_Q \equiv (\Delta_{GL}\hat{Q}_{i,PPV})/\hat{Q}_{i,PPV,L}$ for different ion species (rows of sub-figures) against different parameters (columns of sub-figures).

Global effects arise when some radial profile length scale $L_X = -|\nabla \ln X|^{-1}$ becomes comparable with the orbit width $w_o^{(r)}$, that is $\delta_X = w_o^{(r)}/L_X = \mathcal{O}(1)$. In our case it is the density for which this happens, thus it is instructive to measure the magnitude of global effects against δ_n . A representative value of the maximum δ_n in the profile is given by $\delta_n^* = (w_o/n_0) \frac{\Delta n}{\Delta \psi_N}$, where $w_o = R \frac{\sqrt{2emT}}{Ze\psi_a}$ is a typical trapped orbit width measured in ψ_N (in contrast with $w_o^{(r)}$ that has the dimension of length), with ψ_a denoting ψ at the LCFS, and $n_0 = (n_{Ped} + n_{LCFS})/2$ is the average pedestal density. Note that the density length scale is typically comparable to the pedestal width w , but these quantities can, in general, differ significantly, as is the case in our scans. To take an extreme example, in the scan shown in Fig. 2f, even though w and the density gradient are constant, the logarithmic density gradient, and thus the density scale length, change significantly due to changes in the density. It is thus also interesting to consider the effect of the ratio between the orbit width and the pedestal width, w_o/w , as another possible indicator of globality. For completeness, we also consider the effect of $\Delta n/n_0$. The three parameters considered are chosen such that they increase for pedestals where stronger global effects are expected, and can be related to each other by

$$\delta_n^* = \frac{w_o}{w} \frac{\Delta n}{n_0}. \quad (5)$$

The δ_n^* dependence of the relative variation of the PPV ion heat fluxes, Δ_Q , is shown in the first column of Fig. 7. Below a certain δ_n^* (≈ 0.2 , but increasing with isotope mass) global effects tend to increase Q_i ($\Delta_Q > 0$), while Δ_Q remains below 0.1. As δ_n^* is increased, global effects start to lead to a reduction Q_i . The observed Δ_Q values here occupy a range between 0 and some negative envelope. This envelope first increases in magnitude with δ_n^* then it goes to saturation. Both the δ_n^* value where this saturation occurs, and the corresponding maximum relative reduction in the heat flux, increase with isotope mass. The saturation is observed at $\delta_n^* \approx 0.3$ ($\delta_n^* \approx 0.6$) with a value $\Delta_Q \approx -0.12$ ($\Delta_Q \approx -0.22$) for H (T). It is worth pointing out that the naively expected mass scaling through the orbit

width is already accounted for by defining $\delta_n^* \propto w_o$. That the maximum reduction of Q_i due to global effects is larger for the heavier isotopes represents a favorable trend with isotope mass.

Some of the symbols in Fig. 7 are color coded. The pedestal with the largest δ_n^* (with the highest logarithmic gradient) is black. Shades of red correspond to decreasing δ_n^* from its maximum value by increasing the average pedestal density while keeping the pedestal gradient and the pedestal width fixed (similar to Fig. 2f). In such a scan, Δ_Q increases slowly and monotonically as a function of δ_n^* . Shades of blue correspond to decreasing δ_n^* by making the pedestal wider, while keeping the pedestal top and the LCFS densities fixed (similarly to Fig. 2a). These cases are closer to the lower envelope of the Δ_Q range, which exhibits the saturation. Purple shades correspond to a scan in which both the pedestal width and the average density are changed, as a superposition of the above mentioned extreme cases.

It is interesting to examine, whether one of the factors in δ_n^* , namely w_o/w or $\Delta n/n_o$, is more strongly correlated with global effects than the other, or even with δ_n^* . We find that the correlation of Δ_Q with w_o/w is less clear than it was for δ_n^* , as seen in the second column of Fig. 7. We see that at low values of w_o/w the global effects are weaker in magnitude, but in general we find large scatter in the results for a given value of w_o/w .

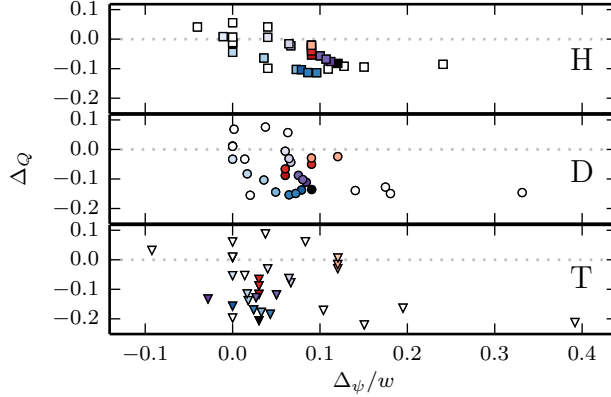
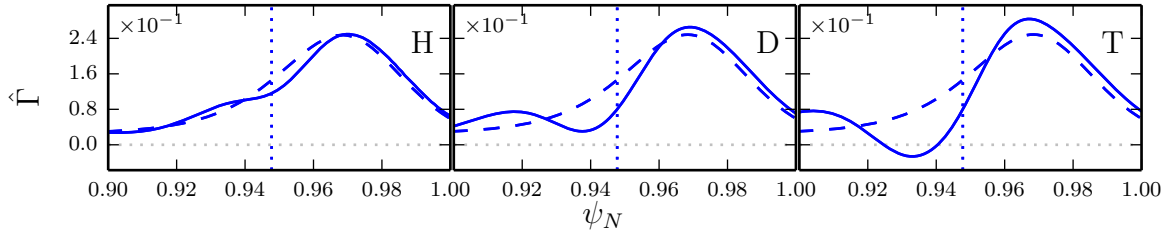
Finally we consider the effect of $\Delta n/n_o$, shown in the last column of Fig. 7. As mentioned, at lower values of this parameter Q_i is increased by the global effects. When $\Delta n/n_o > 0.8$, we mostly see negative values of Δ_Q with a large scatter and no clear trends.

As another measure of global effects besides Δ_Q , we may also consider the difference in the ψ_N locations of the peaks between global and local heat flux results, which we denote by Δ_ψ . Unless there is a substantial radiative energy loss in the pedestal, with sharp radial variation, the location of the maximum neoclassical heat flux should approximately coincide with the region of strongest reduction in the ion scale turbulent fluctuation levels, which in turn, may be measurable with certain fluctuation diagnostics. Positive values of Δ_ψ indicate that the global neoclassical heat flux peaks at a larger radius than the local flux. To be able to sensibly compare effects in pedestals with different width w we show $\Delta_\psi/w \in [-1, 1]$ in Fig. 8.

We find that the location of the PPV heat flux is shifted outward in most cases, as seen in the first column of Fig. 8. However, there are a few cases when it is shifted inwards. With increasing δ_n^* the positive range of Δ_ψ/w values increases up to the δ_n^* where the saturation of Δ_Q occurred, then the range shrinks again. As the δ_n^* point where the trend in the Δ_ψ/w changes increases with isotope mass, the maximum possible Δ_ψ/w value is also significantly larger for heavier isotopes.

The second column of Fig. 8 shows the w_o/w dependence of Δ_ψ/w . Although in most of the cases we see only a weak positive shift, there are significant shifts of the heat flux peak location towards the separatrix; and the range of Δ_ψ/w keeps increasing with w_o/w . This approximate proportionality of the envelope of the Δ_ψ/w data to w_o/w is related to the appearance of the $1/w$ factor in both quantities. Reducing the pedestal width (i.e. increasing w_o/w) can sharpen the pedestal, which would intuitively make non-local effects stronger, while the observed increase in the maximum relative shift Δ_ψ/w is consistent with the trivial effect from the $1/w$ factor.

The effect of $\Delta n/n_o$ on Δ_ψ/w is shown in the third column of Fig. 8. We see a few inward shifts of the peak Q_i location, but mostly find outward shifts. We observe the strongest outward shift for all species somewhat above $\Delta n/n_o = 0.94$, and at higher values of $\Delta n/n_o$ we see a decreasing trend in the maximum outward shifts. Interestingly the rate of this reduction is faster in heavier isotopes. The largest outward shift is only ≈ 2 times higher for H than the shift in the largest δ_n^* simulation at $\Delta n/n_o \approx 1.68$ (black symbols), in contrast to the factor of ≈ 11.9 difference between the corresponding pair of points for T. This may relate to the curious fact that when the pedestal width is decreased for fixed $\Delta n/n_o \approx 1.68$ (symbols with blue shades) the relative outward shift of the Q_i peak is increasing for sharper pedestals for H, while for T the Δ_ψ/w points in this scan almost overlap, due to the lower envelope.

FIG. 9: Δ_Q plotted against Δ_ψ/w for different isotopes.FIG. 10: Normalized particle flux $\hat{\Gamma}$ for the baseline profile (blue in Fig. 2) in H, D and T plasmas. Solid (dashed) curves are from global (local) simulations.

Next we consider possible correlations between Δ_Q and Δ_ψ/w ; these quantities are plotted against each other in Fig. 9. Although we observe that Δ_Q tend to be negative for the highest values of Δ_ψ/w , and positive for the highest negative values of Δ_ψ/w , we do not see a clear correlation between these quantities. It is interesting though, that the three color coded scans show different behaviors for the various species. In particular the highest δ_n^* pedestal (black symbols) becomes close to the observed maximum Δ_Q value when going from H to T, while Δ_ψ/w is significantly reduced.

D. Particle and momentum fluxes

Unlike in the plasma core, due to the presence of strong gradients, neoclassical particle transport can be non-negligible in the pedestal, in the sense that $T\Gamma_i \sim Q_i$, even if impurities are only present in trace quantities.

In previous studies^{27,33,40}, the global drift kinetic equation (1) has usually been solved together with the constraints $\langle \int d^3v g \rangle = \langle \int d^3v v^2 g \rangle = 0$, to obtain the radial dependence of two components of S , corresponding to particle and energy sources. However, S did not contribute to the angular momentum balance. This method, in general, does not lead to ambipolar fluxes, $\sum_a Z_a e \Gamma_a = 0$. In the current work we allow for an additional component in S , corresponding to an angular momentum source, and this degree of freedom is used to enforce ambipolarity, as explained in Appendix A and in Appendix C of Ref. 33. Accordingly, the particle fluxes shown in Fig. 10 are the same for ions and electrons. Note that the peak particle fluxes reach values of $\hat{\Gamma} \approx 0.31$, that is indeed comparable to \hat{Q} in Fig. 5. Thus, a significant fraction of the energy flux is convective (while it is often assumed to be dominantly conductive^{41–43}).

Like the energy flux, the deviation between local and global particle fluxes increases with

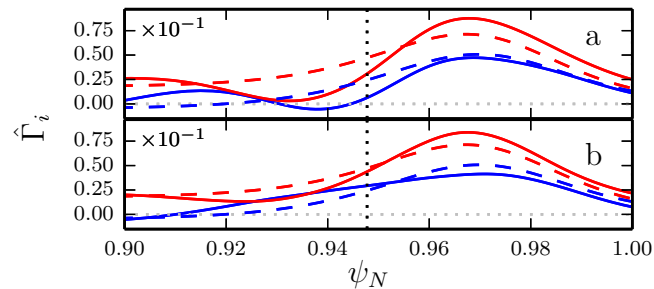


FIG. 11: Normalized particle fluxes $\hat{\Gamma}$ for the baseline profile with 1:1 D-T mixture. Blue (red) are deuterium (tritium) fluxes. (a): momentum sources proportional to particle mass; (b): ambipolarity enforced without electron momentum sources, ion momentum sources proportional to their mass. Solid (dashed) curves are from global (local) simulations.

isotope mass. While the global effects are quite weak for H, we find a non-negligible increase in the peak value of $\hat{\Gamma}$, and an even more pronounced reduction inside the pedestal top for T. Thus, a significant part of the global reduction of \hat{Q} in the near-pedestal core is due to a reduced convective heat flux, while the reduction of \hat{Q} in the pedestal corresponds to a slight increase in convective and a stronger decrease in conductive heat flux. The tritium particle flux even changes sign at $\psi_N \approx 0.94$. Note that the global modifications to the particle flux are similarly strong for electrons, since the fluxes are ambipolar. This strong non-local behavior for electrons depends on whether and how ambipolarity is enforced, i.e. it is not a result of direct orbit width effects, which are negligible for electrons. The question of ambipolarity and momentum sources in relation to the particle transport are discussed in Appendix A. The specific choices made here are not expected to have major impact on the results of the previous section, as the peak value of the particle flux is less sensitive than the that of the ion heat flux with respect to the ion mass; that is, the isotope dependence of the heat flux is dominated by the conductive component.

Nevertheless, different isotopes having different particle fluxes has potential implications for mixtures in the form of isotope separation. For instance the ion concentrations in a D-T fusion plasma can shift away from the ideal 1:1 ratio. That different isotopes in a mixture are transported differently has long been known, see e.g. Ref. 44 for analytic theory relevant to the local banana-regime.

To investigate how this is modified by global effects, we performed simulations of H-D and D-T 1:1 mixtures, with the ion densities taken as half the baseline electron density. Fig. 11 depicts the resulting particle fluxes. As the global fluxes depend on how ambipolarity is restored, we performed simulations with electron sources, similar to the pure simulations (Fig. 11a), and without electron sources (Fig. 11b). We first consider the local particle fluxes (dashed lines, which are the same in both Fig. 11a and b). In the core the electron flux is small, thus the ion components are transported in opposite directions; the D (T) flows are inward (outward). As the electron profile gradients increase towards the pedestal and Γ_e becomes non-negligible (and outward) both D and T are transported outward but on different rates; the T flux being larger. Finally, as the ion collisionality decreases towards the edge (due to the strong density drop and flat ion temperature profile), the D and T fluxes get closer to each other.

Sufficiently far from the pedestal the global simulation results approach the local ones, while closer to the pedestal ($\psi_N \approx 0.92$) the deuterium and tritium fluxes approach each other, and then diverge from each other. Inside most of the pedestal the T flux is even larger than that in the local simulation, while the D flux is somewhat lower, increasing the disparity between these fluxes. These features occur independently of whether electron momentum sources are allowed or not. In the simulations with electron momentum sources the individual ion fluxes for the two isotopes resemble the corresponding single species

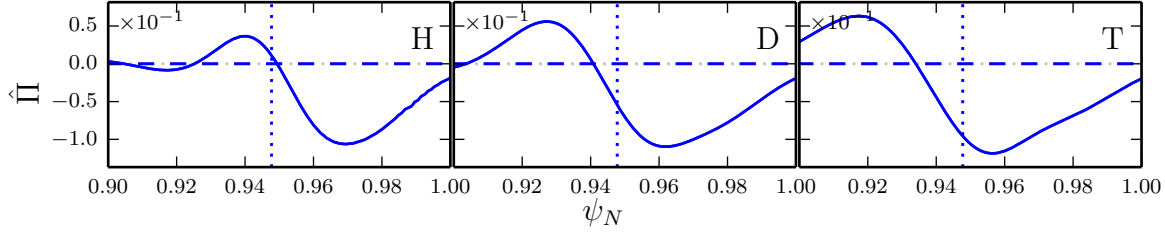


FIG. 12: Normalized total angular momentum flux $\hat{\Pi}$ for the baseline profile (blue in Fig. 2) in H, D and T plasmas. Solid (dashed) curves are from global (local) simulations.

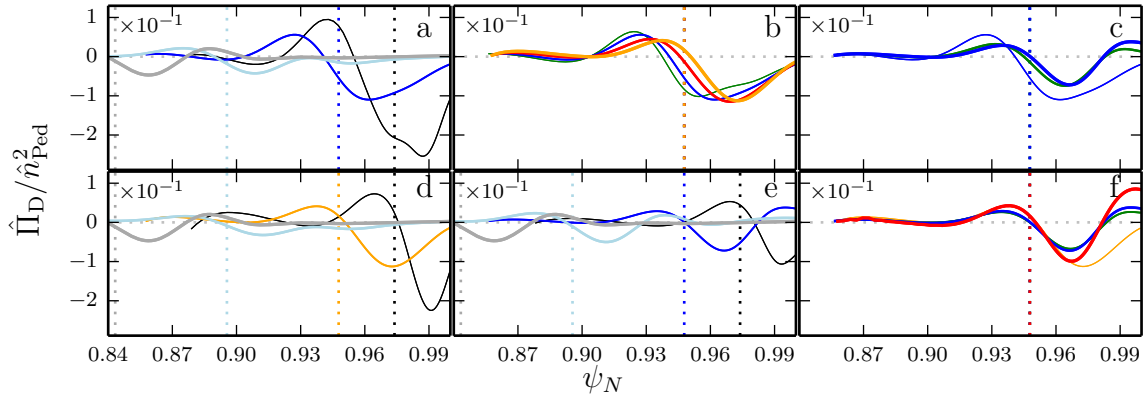


FIG. 13: Angular momentum flux normalized as $\hat{\Pi}_D / \hat{n}_{Ped}^2$ from deuterium simulations using the profiles in Fig. 2. Solid (dashed) curves are from global (local) simulations.

Thinner lines correspond to sharper or narrower pedestals in the scan.

results; compare to the last two panels of Fig. 10). In the simulation with no electron momentum sources, they should add up to produce the approximately local electron result, therefore the deviations from their local results has to mirror each other. This has the most significant effect in the near pedestal core, especially for the D flux: while it changes sign around $\psi_N \approx 0.94$ with electron momentum source, it remains positive without it. Regardless of these details, as the isotopes are transported differently in both local and global simulations with a larger outward T flux, they are prone to develop different density profiles in experiments, and their fueling may need to be adjusted to optimize the isotope ratio in the deep core.

As for the angular momentum transport, it cannot be sensibly evaluated in the lowest order local theory as it is a higher order effect. Indeed, in our local simulations the angular momentum transport evaluates to zero. However, as it was pointed out in Ref. 45, momentum transport in the pedestal due to finite orbit width effects is not only non-negligible, but it translates to experimentally relevant Prandtl number estimates.

First we consider the isotope scaling of momentum transport for our baseline profiles, shown in Fig. 12. As expected, the local values are identically zero, while we find an inward flux of co-current (i.e. ion-diamagnetic direction) angular momentum inside the pedestal, and a somewhat weaker outward flux in the near-pedestal core. In the simulations the radial variation of these momentum fluxes is balanced by momentum sources. (Note that qualitatively similar momentum fluxes were reported³³ in simulations without momentum sources, where a torque from finite radial currents played the role of momentum sources). Observe that, according to our definition of $\hat{\Pi}$ given above Eq. (4), the angular momentum transport is $\propto m\hat{\Pi}$. The toroidal ion flow can be viewed as a drive for the momentum flux, and its $E \times B$ and diamagnetic components are mass independent. Nevertheless,

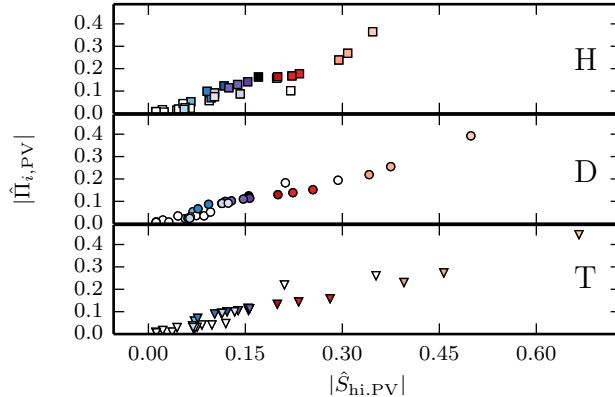


FIG. 14: Pedestal peak values of the momentum flux $\hat{\Pi}$ and the heat source S_h .

it is somewhat unexpected that the largest negative value of $\hat{\Pi}$ in the pedestal does not increase significantly in magnitude with increasing isotope mass, since the momentum flux we observe is a finite orbit width effect. However, the largest positive value of $\hat{\Pi}$, inward of the pedestal top, does increase in both magnitude and its extent towards the core.

Finally, the effect of varying the pedestal parameters on angular momentum transport is considered; $\hat{\Pi}/\hat{n}_{\text{Ped}}^2$ is shown in Fig. 13 for the various density profile scans of Fig. 2 in a D plasma. The strongest momentum transport is observed for the highest δ_n^* case, corresponding to the narrowest pedestal in Fig. 2a. In this scan, where the position of the pedestal top is shifted inward, we observe a rather strong reduction in the largest negative value of Π (in the following discussion we will simply refer to it as the peak Π) as the gradient decreases. The location of the peak is shifted outward so that it stays in the vicinity of the pedestal top; in the shallower pedestals Π is small in most of the pedestal, except close to the pedestal top. We note that for the model T_i profile used here, the abrupt increase of $dT_i/d\psi$ close to the pedestal top usually leads to more pronounced global effects in that region, correlated with a peaking of sources. We observe a localization of momentum sources around the pedestal top in all scans when the pedestal width is changing; see also Fig. 13d and e.

The n^2 scaling of the local heat fluxes in the banana regime was a useful guide to choose a convenient normalizing factor, $1/\hat{n}_{\text{Ped}}^2$, in Fig. 6. For momentum fluxes such simple guidance is not available, as the lowest order local momentum fluxes are zero. However, whilst heat sources (in the form of a radial variation of turbulent transport fluxes and actual heat sources) may be expected to be in proportion to the heat fluxes, heat sources will also represent an important contribution to finite orbit width momentum fluxes, as shown in the higher order theory of Ref. 46). Therefore it is reasonable to assume an n^2 scaling for Π as well; indeed, with the $1/\hat{n}_{\text{Ped}}^2$ normalization we observe comparable peak values of the momentum transport over the wide range of \hat{n}_{Ped} values in the scans of Fig. 2b and f, as seen in the corresponding Fig. 13b and f. In particular, apart from an inward shift of the peak Π location as \hat{n}_{Ped} increases, we find very similar peak values of $\hat{\Pi}/\hat{n}_{\text{Ped}}^2$ in Fig. 13b.

To more clearly show that the momentum fluxes and the heat sources are strongly correlated we plot the largest observed momentum fluxes against the largest sources (considering only the magnitude of these quantities) for all our simulations in Fig. 14; here, we plot the *peak value* (PV), which differs from the PPV in that the peak is allowed to be outside the pedestal. We find an approximate proportionality with a slope that is almost mass independent [linear fits give coefficients of 0.86 ± 0.06 (H), 0.68 ± 0.04 (D), and 0.67 ± 0.04 (T)]. We have normalized $\hat{\Pi}$ and \hat{S} such that this mass independence translates to $\Pi \propto m \int d^3v mv^2 S$, where Π is the radial transport of angular momentum and S is the source appearing in the kinetic equation (1), that conforms qualitatively with the source contribution in Eq. (104) of Ref. 46. This is potentially important, because sources in the pedestal are much larger than

in the core, as the radial variation of the fluxes in the various transport channels happens on a short radial scale.

IV. SUMMARY

We have studied cross field fluxes of heat, particles and momentum in sharp density pedestals. We focused on differences between radially *local* and *global* simulation results. The deviations between local and global results depend on isotopic mass, and on features of the plasma parameter profiles. This study considers isotope effects for fixed pedestal profiles, and the impact of changing the shape of the density pedestal. We parametrize the pedestal by four parameters – the densities at the pedestal top and at the last closed flux surface, the representative pedestal gradient, and the pedestal width – three of which are independent.

For both particle and heat fluxes we see a clear increase in global effects with increasing isotope mass, owing to an increasing thermal ion orbit width. Not only does the deviation between local and global results increase inside the pedestal, but so does the distance over which global effects penetrate into the core. The global particle flux is found to be particularly sensitive to isotope effects: when electron momentum sources are allowed the tritium particle flux is strongly reduced in the near-pedestal core region, even changing sign, due to global effects. When only the ions are allowed to have momentum sources, the global particle flux remain close to the local one. However in isotope mixtures and impure plasmas the various ion components may exhibit deviations from local results, as long as ambipolarity is satisfied.

Even though the angular momentum transport is purely a finite orbit width effect (it vanishes in the lowest order local theory), it does not exhibit a strong isotopic dependence, apart from its trivial proportionality with mass (in the sense that, if momentum diffusivity could be sensibly defined it would approximately be mass independent).

In a scan where the pedestal width and the LCFS density are fixed and the pedestal top density is increased, we see only weak changes in globality. Perhaps more surprisingly, we find that in a scan where the pedestal top density and location is changed keeping the representative gradient in the pedestal fixed, thin pedestals can be much more global than wider ones. Although we only considered steady state profiles, this scan may be relevant in the growth phase of ballooning mode limited pedestals, when the large gradient region gradually expands into the core, while the pedestal pressure gradient is approximately constant. These observations indicate the role of the density length scale in affecting globality.

Since experimental ion heat fluxes have been found to be consistent with being purely neoclassical in some cases, the peak ion heat flux and its location within the pedestal are of interest. The relative changes in these two quantities due to global effects are used here to quantify globality. We studied their dependence on three pedestal shape parameters: the ratio of the ion orbit width and the density length scale, δ_n^* , the ratio of the orbit width and the pedestal width, w_o/w , and the relative density drop in the pedestal $\Delta n/n_0$. We found that, the peak ion heat flux is mostly reduced and it is shifted outward by global effects (these are modest changes but they might be measurable). The clearest correlation was found with δ_n^* . Even though δ_n^* accounts for the mass dependence through the ion orbit width, we find additional differences between the various isotopes. The range of possible reductions in the heat flux peak saturates at some value of δ_n^* . Importantly, this value and the corresponding maximum reduction of the heat flux increases with mass, representing a favorable isotope scaling trend. Finally, we find that the flux of radial angular momentum is strongly correlated with the heat sources that appear in the simulation to sustain the steady state pedestal profiles.

ACKNOWLEDGMENTS

We are grateful to S.L. Newton and J.T. Omotani for valuable comments on our manuscript, and to M. Landreman for providing the PERFECT code. The research was supported by the International Career Grant of Vetenskapsrådet (Dnr. 330-2014-6313) and Marie Skłodowska Curie Actions, Cofund, Project INCA 600398. The simulations used SNIC computational resources at Kabnekaise (Dnr: 2017/3-29) and Hebbe (Dnr: 2017/1-95).

Appendix A: Momentum sources and ambipolarity

In the local theory $\delta f = f - f_M \ll f_M$ and $\nabla \ln \delta f \sim \nabla \ln f_M$, thus $\nabla \delta f \ll \nabla f_M$, while in the global theory adopted here δf can develop sharp features radially, so that $\nabla \delta f \sim \nabla f_M$. Accordingly, $\nabla \delta f$ needs to be retained one order lower than usually. Noting that the cross field fluxes are evaluated at fix particle (as opposed to guiding center) position, these global orderings lead to an enhancement of the gyrophase dependent $-\boldsymbol{\rho} \cdot \nabla f$ term. This leads to that a finite angular momentum appears already in the order we solve for δf , even though we assume subsonic ion flows.

From the steady-state, species-summed, flux-surface averaged momentum conservation equation, it follows that the radial flux of toroidal angular momentum is balanced by radial currents and/or momentum sources. The global simulations are not intrinsically-ambipolar, thus if ambipolarity is not enforced radial currents arise. To be consistent with ambipolarity these currents should be balanced by other non-intrinsically-ambipolar processes which are outside the physics modeled by the code (e.g. ripple losses). However, as shown in Ref. 33, the ambipolarity of the neoclassical radial particle flux can be enforced. Since requiring ambipolarity $\sum_a Z_a e \Gamma_a = 0$ only yields one additional ψ -dependent constraint (as opposed to one constraint per species), the distribution of the momentum source among the various species represents some degree of freedom, in addition to the freedom of specifying the poloidal and velocity dependences of all the sources.

In the simulations presented in this paper, the momentum source is uniform in the poloidal angle, and it is distributed to the species in proportion to their mass; specifically, the momentum source in the equation for species a , S_{ma} is given by

$$S_{ma} = \hat{m}_a V_a(\mathbf{v}) S_m(\psi) \quad (\text{A1})$$

where $V_a(\mathbf{v}) = \xi x(x^2 - 7/2)e^{-x^2}$, with $x = v/v_{Ta}$ and $\xi = v_{\parallel}/v$.

As a result of allowing for momentum source to the electrons (albeit small in mass ratio, so that the neoclassical parallel currents are not strongly modified), the electron particle fluxes in Fig. 10 become non-local, and are similar to the ion fluxes in the non-intrinsically-ambipolar simulations of Ref. 33. On the other hand, if the momentum sources of electrons are set to zero, the electron particle fluxes remain much closer to the local result (shown by the bright lines in Fig. 15), as expected when collisional coupling to the ions is weak. As a consequence, the particle fluxes in pure D or T plasmas (light blue) are forced to be local to satisfy ambipolarity, and become essentially isotope independent. However, in mixture plasmas the ion components can deviate from the local result, as only the total ion flux should be the same as the (very nearly local) electron flux.

¹J. Jacquinet, V. Bhatnagar, J. Cordey, L. Horton, D. Start, R. Barnsley, P. Breger, J. Christiansen, S. Clement, S. Davies, J. Ehrenberg, L.-G. Eriksson, G. Fishpool, M. Gadeberg, P. Harbour, H. Jckel, K. Lawson, J. Lingertat, C. Lowry, C. Maggi, G. Matthews, R. Monk, D. O'Brien, E. Righi, G. Saibene, R. Sartori, B. Schunke, A. Sips, M. Stamp, D. Stork, J. Strachan, A. Tanga, K. Thomsen, and the JET Team, "Overview of ITER physics deuterium-tritium experiments in JET," Nuclear Fusion **39**, 235 (1999).

²J. D. Strachan, S. Batha, M. Beer, M. G. Bell, R. E. Bell, A. Belov, H. Berk, S. Bernabei, M. Bitter, B. Breizman, N. L. Bretz, R. Budny, C. E. Bush, J. Callen, S. Cauffman, C. S. Chang, Z. Chang, C. Z. Cheng, D. S. Darrow, R. O. Dendy, W. Dorland, H. Duong, P. C. Efthimion, D. Ernst, H. Evenson, N. J. Fisch, R. Fisher, R. J. Fonck, E. D. Fredrickson, G. Y. Fu, H. P. Furth, N. N. Gorelenkov, V. Y.

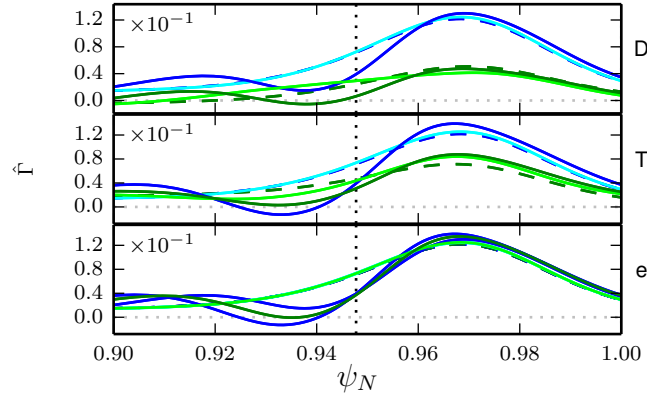


FIG. 15: Normalized particle flux $\hat{\Gamma}$ for the baseline profile with pure D and T plasma (blue) and a 1:1 D-T mixture (green). Solid (dashed) curves are from global (local) simulations. Lighter shades corresponds to simulations with no momentum source to electrons.

- Goloborod'ko, B. Grek, L. R. Grisham, G. W. Hammett, R. J. Hawryluk, W. Heidbrink, H. W. Herrmann, M. C. Herrmann, K. W. Hill, J. Hogan, B. Hooper, J. C. Hosea, W. A. Houlberg, M. Hughes, D. L. Jassby, F. C. Jobes, D. W. Johnson, R. Kaita, S. Kaye, J. Kesner, J. S. Kim, M. Kissick, A. V. Krasilnikov, H. Kugel, A. Kumar, N. T. Lam, P. Lamarche, B. Leblanc, F. M. Levinton, C. Ludescher, J. Machuzak, R. P. Majeski, J. Manickam, D. K. Mansfield, M. Mauel, E. Mazzucato, J. McChesney, D. C. McCune, G. McKee, K. M. McGuire, D. M. Meade, S. S. Medley, D. R. Mikkelsen, S. V. Mirnov, D. Mueller, Y. Nagayama, G. A. Navratil, R. Nazikian, M. Okabayashi, M. Osakabe, D. K. Owens, H. K. Park, W. Park, S. F. Paul, M. P. Petrov, C. K. Phillips, M. Phillips, P. Phillips, A. T. Ramsey, B. Rice, M. H. Redi, G. Rewoldt, S. Reznik, A. L. Roquemore, J. Rogers, E. Ruskov, S. A. Sabbagh, M. Sasao, G. Schilling, G. L. Schmidt, S. D. Scott, I. Semenov, T. Senko, C. H. Skinner, T. Stevenson, E. J. Strait, B. C. Stratton, W. Stodiek, E. Synakowski, H. Takahashi, W. Tang, G. Taylor, M. E. Thompson, S. von Goeler, A. von Halle, R. T. Walters, S. Wang, R. White, R. M. Wieland, M. Williams, J. R. Wilson, K. L. Wong, G. A. Wurden, M. Yamada, V. Yavorski, K. M. Young, L. Zakharov, M. C. Zarnstorff, and S. J. Zweben, "TFTR DT experiments," *Plasma Physics and Controlled Fusion* **39**, B103 (1997).
- ³M. Shimada, D. Campbell, V. Mukhovatov, M. Fujiwara, N. Kirneva, K. Lackner, M. Nagami, V. Pustovitov, N. Uckan, J. Wesley, N. Asakura, A. Costley, A. Donn, E. Doyle, A. Fasoli, C. Gormezano, Y. Gribov, O. Gruber, T. Hender, W. Houlberg, S. Ide, Y. Kamada, A. Leonard, B. Lipschultz, A. Loarte, K. Miyamoto, V. Mukhovatov, T. Osborne, A. Polevoi, and A. Sips, "Chapter 1: Overview and summary," *Nuclear Fusion* **47**, S1 (2007).
- ⁴A. C. C. Sips, G. Giruzzi, S. Ide, C. Kessel, T. C. Luce, J. A. Snipes, and J. K. Stober, "Progress in preparing scenarios for operation of the international thermonuclear experimental reactor," *Physics of Plasmas* **22**, 021804 (2015), <http://dx.doi.org/10.1063/1.4904015>.
- ⁵J. Q. Dong, W. Horton, and W. Dorland, "Isotope scaling and η_i mode with impurities in tokamak plasmas," *Physics of Plasmas* **1**, 3635–3640 (1994), <http://dx.doi.org/10.1063/1.870942>.
- ⁶D. R. Ernst, B. Coppi, S. D. Scott, M. Porkolab, and TFTR Group, "Unifying role of radial electric field shear in the confinement trends of TFTR supershot plasmas," *Phys. Rev. Lett.* **81**, 2454–2457 (1998).
- ⁷G. Bateman, A. H. Kritz, V. V. Parail, and J. G. Cordey, "Effect of isotope mass on transport simulations of Joint European Torus high-mode plasmas with Edge Localized Modes," *Physics of Plasmas* **6**, 4607–4614 (1999), <http://dx.doi.org/10.1063/1.873724>.
- ⁸M. Z. Tokar, D. Kalupin, and B. Unterberg, "Nature of the isotope effect on transport in tokamaks," *Phys. Rev. Lett.* **92**, 215001 (2004).
- ⁹C. Estrada-Mila, J. Candy, and R. E. Waltz, "Gyrokinetic simulations of ion and impurity transport," *Physics of Plasmas* **12**, 022305 (2005), <http://dx.doi.org/10.1063/1.1848544>.
- ¹⁰I. Pusztai, J. Candy, and P. Gohil, "Isotope mass and charge effects in tokamak plasmas," *Physics of Plasmas* **18**, 122501 (2011).
- ¹¹A. Bustos, A. B. Navarro, T. Görler, F. Jenko, and C. Hidalgo, "Microturbulence study of the isotope effect," *Physics of Plasmas* **22**, 012305 (2015), <http://dx.doi.org/10.1063/1.4905637>.
- ¹²Y. Shen, J. Q. Dong, A. P. Sun, H. P. Qu, G. M. Lu, Z. X. He, H. D. He, and L. F. Wang, "Isotope effects of trapped electron modes in the presence of impurities in tokamak plasmas," *Plasma Physics and Controlled Fusion* **58**, 045028 (2016).
- ¹³M. Nakata, M. Nunami, H. Sugama, and T.-H. Watanabe, "Impact of hydrogen isotope species on microinstabilities in helical plasmas," *Plasma Physics and Controlled Fusion* **58**, 074008 (2016).
- ¹⁴W. Guo, L. Wang, and G. Zhuang, "Impurity effects on residual zonal flow in deuterium (D)-tritium (T)

- plasmas,” *Nuclear Fusion* **57**, 056012 (2017).
- ¹⁵C. Holland, “Validation metrics for turbulent plasma transport,” *Physics of Plasmas* **23**, 060901 (2016), <http://dx.doi.org/10.1063/1.4954151>.
- ¹⁶M. Bessenrodt-Weberpals, F. Wagner, O. Gehre, L. Giannone, J. Hofmann, A. Kallenbach, K. McCormick, V. Mertens, H. Murmann, F. Ryter, B. Scott, G. Siller, F. Soldner, A. Stabler, K.-H. Steuer, U. Stroth, N. Tsois, H. Verbeek, and H. Zohm, “The isotope effect in ASDEX,” *Nuclear Fusion* **33**, 1205 (1993).
- ¹⁷R. J. Hawryluk, “Results from deuterium-tritium tokamak confinement experiments,” *Rev. Mod. Phys.* **70**, 537–587 (1998).
- ¹⁸J. Jacquinot and the JET team, “Deuterium-tritium operation in magnetic confinement experiments: results and underlying physics,” *Plasma Physics and Controlled Fusion* **41**, A13 (1999).
- ¹⁹S. D. Scott, M. C. Zarnstorff, C. W. Barnes, R. Bell, N. L. Bretz, C. Bush, Z. Chang, D. Ernst, R. J. Fonck, L. Johnson, E. Mazzucato, R. Nazikian, S. Paul, J. Schivell, E. J. Synakowski, H. Adler, M. Bell, R. Budny, E. Fredrickson, B. Grek, A. Janos, D. Johnson, D. McCune, H. Park, A. Ramsey, M. H. Redi, G. Taylor, M. Thompson, and R. Wieland, “Isotopic scaling of confinement in deuterium-tritium plasmas,” *Physics of Plasmas* **2**, 2299–2307 (1995), <http://dx.doi.org/10.1063/1.871253>.
- ²⁰D. Schissel, K. Burrell, J. DeBoo, R. Groebner, A. Kellman, N. Ohyabu, T. Osborne, M. Shimada, R. Snider, R. Stambaugh, T. Taylor, and DIII-D Research Team, “Energy confinement properties of h-mode discharges in the DIII-D tokamak,” *Nuclear Fusion* **29**, 185 (1989).
- ²¹C. Maggi, “Isotope effects on L-H threshold and confinement in tokamak plasmas,” (Contribution to the 44th EPS Conference on Plasma Physics, 15.013, 2017).
- ²²J. Cordey, B. Balet, D. Bartlett, R. Budny, J. Christiansen, G. Conway, L.-G. Eriksson, G. Fishpool, C. Gowers, J. de Haas, P. Harbour, L. Horton, A. Howman, J. Jacquinot, W. Kerner, C. Lowry, R. Monk, P. Nielsen, E. Righi, F. Rimini, G. Saibene, R. Sartori, B. Schunke, A. Sips, R. Smith, M. Stamp, D. Start, K. Thomsen, B. Tubbing, and M. von Hellermann, “Plasma confinement in JET H-mode plasmas with H, D, DT and T isotopes,” *Nuclear Fusion* **39**, 301 (1999).
- ²³C. Maggi, S. Saarelma, F. Casson, C. Challis, E. de la Luna, L. Frassinetti, C. Giroud, E. Joffrin, J. Simpson, M. Beurskens, I. Chapman, J. Hobirk, M. Leyland, P. Lomas, C. Lowry, I. Nunes, F. Rimini, A. Sips, and H. Urano, “Pedestal confinement and stability in JET-ILW ELMy H-modes,” *Nuclear Fusion* **55**, 113031 (2015).
- ²⁴J. Omotani, I. Pusztai, S. Newton, and T. Fülöp, “Plasma rotation from momentum transport by neutrals in tokamaks,” *Nuclear Fusion* **56**, 124002 (2016).
- ²⁵P. Snyder, R. Groebner, J. Hughes, T. Osborne, M. Beurskens, A. Leonard, H. Wilson, and X. Xu, “A first-principles predictive model of the pedestal height and width: development, testing and iter optimization with the eped model,” *Nuclear Fusion* **51**, 103016 (2011).
- ²⁶M. Landreman and D. R. Ernst, “Local and global Fokker-Planck neoclassical calculations showing flow and bootstrap current modification in a pedestal,” *Plasma Physics and Controlled Fusion* **54**, 115006 (2012).
- ²⁷M. Landreman, F. I. Parra, P. J. Catto, D. R. Ernst, and I. Pusztai, “Radially global δf computation of neoclassical phenomena in a tokamak pedestal,” *Plasma Physics and Controlled Fusion* **56**, 045005 (2014), [arXiv:1312.2148 \[physics.plasm-ph\]](https://arxiv.org/abs/1312.2148).
- ²⁸S. K. Wong and V. S. Chan, “Numerical solution of neoclassical ion transport using the Fokker-Planck operator for coulomb collisions,” *Plasma Physics and Controlled Fusion* **53**, 095005 (2011).
- ²⁹E. A. Belli and J. Candy, “Full linearized Fokker-Planck collisions in neoclassical transport simulations,” *Plasma Physics and Controlled Fusion* **54**, 015015 (2012).
- ³⁰C. S. Chang, S. Ku, G. R. Tynan, R. Hager, R. M. Churchill, I. Cziegler, M. Greenwald, A. E. Hubbard, and J. W. Hughes, “Fast low-to-high confinement mode bifurcation dynamics in a tokamak edge plasma gyrokinetic simulation,” *Phys. Rev. Lett.* **118**, 175001 (2017).
- ³¹E. Viezzer, T. Pütterich, R. M. McDermott, G. D. Conway, M. Cavedon, M. G. Dunne, R. Dux, E. Wolfrum, and the ASDEX Upgrade Team, “Parameter dependence of the radial electric field in the edge pedestal of hydrogen, deuterium and helium plasmas,” *Plasma Physics and Controlled Fusion* **56**, 075018 (2014).
- ³²C. Theiler, J. L. Terry, E. Edlund, I. Cziegler, R. M. Churchill, J. W. Hughes, B. LaBombard, T. Golfopoulos, and the Alcator C-Mod Team, “Radial localization of edge modes in alcator c-mod pedestals using optical diagnostics,” *Plasma Physics and Controlled Fusion* **59**, 025016 (2017).
- ³³S. Buller, I. Pusztai, S. L. Newton, and J. T. Omotani, “Neoclassical flows in deuterium-helium plasma density pedestals,” *Plasma Physics and Controlled Fusion* **59**, 055019 (2017).
- ³⁴M. N. A. Beurskens, T. H. Osborne, P. A. Schneider, E. Wolfrum, L. Frassinetti, R. Groebner, P. Lomas, I. Nunes, S. Saarelma, R. Scannell, P. B. Snyder, D. Zarzoso, I. Balboa, B. Bray, M. Brix, J. Flanagan, C. Giroud, E. Giovannozzi, M. Kempenaars, A. Loarte, E. de la Luna, G. Maddison, C. F. Maggi, D. McDonald, R. Pasqualotto, G. Saibene, R. Sartori, E. R. Solano, M. Walsh, and L. Zabeo, “H-mode pedestal scaling in diii-d, asdex upgrade, and jet,” *Physics of Plasmas* **18**, 056120 (2011), <http://dx.doi.org/10.1063/1.3593008>.
- ³⁵L. Frassinetti, M. Beurskens, S. Saarelma, J. Boom, E. Delabie, J. Flanagan, M. Kempenaars, C. Giroud, P. Lomas, L. Meneses, C. Maggi, S. Menmuir, I. Nunes, F. Rimini, E. Stefanikova, H. Urano, G. Verdoolaege, and JET Contributors, “Global and pedestal confinement and pedestal structure in dimensionless collisionality scans of low-triangularity H-mode plasmas in JET-ILW,” *Nuclear Fusion* **57**, 016012 (2017).

- ³⁶E. Wolfrum, E. Viezzer, A. Burckhart, M. Dunne, P. Schneider, M. Willensdorfer, E. Fable, R. Fischer, D. Hatch, F. Jenko, B. Kurzan, P. Manz, S. Rathgeber, and the ASDEX Upgrade Team, “Overview of recent pedestal studies at ASDEX Upgrade,” *Nuclear Fusion* **55**, 053017 (2015).
- ³⁷E. Viezzer, T. Pütterich, C. Angioni, A. Bergmann, R. Dux, E. Fable, R. McDermott, U. Stroth, E. Wolfrum, and the ASDEX Upgrade Team, “Evidence for the neoclassical nature of the radial electric field in the edge transport barrier of ASDEX Upgrade,” *Nuclear Fusion* **54**, 012003 (2014).
- ³⁸R. L. Miller, M. S. Chu, J. M. Greene, Y. R. Lin-Liu, and R. E. Waltz, “Noncircular, finite aspect ratio, local equilibrium model,” *Physics of Plasmas* **5**, 973–978 (1998).
- ³⁹E. Viezzer, E. Fable, M. Cavedon, C. Angioni, R. Dux, F. Laggner, M. Bernert, A. Burckhart, R. McDermott, T. Pütterich, F. Ryter, M. Willensdorfer, E. Wolfrum, the ASDEX Upgrade Team, and the EUROfusion MST1 Team, “Investigation of inter-ELM ion heat transport in the H-mode pedestal of ASDEX Upgrade plasmas,” *Nuclear Fusion* **57**, 022020 (2017).
- ⁴⁰I. Pusztai, S. Buller, and M. Landreman, “Global effects on neoclassical transport in the pedestal with impurities,” *Plasma Physics and Controlled Fusion* **58**, 085001 (2016).
- ⁴¹I. Pusztai and P. J. Catto, “Neoclassical plateau regime transport in a tokamak pedestal,” *Plasma Physics and Controlled Fusion* **52**, 075016 (2010).
- ⁴²G. Kagan and P. J. Catto, “Neoclassical ion heat flux and poloidal flow in a tokamak pedestal,” *Plasma Physics and Controlled Fusion* **52**, 055004 (2010).
- ⁴³P. J. Catto, F. I. Parra, G. Kagan, J. B. Parker, I. Pusztai, and M. Landreman, “Kinetic effects on a tokamak pedestal ion flow, ion heat transport and bootstrap current,” *Plasma Physics and Controlled Fusion* **55**, 045009 (2013).
- ⁴⁴J. W. Connor, “The neo-classical transport theory of a plasma with multiple ion species,” *Plasma Physics* **15**, 765 (1973).
- ⁴⁵S. Buller, I. Pusztai, and M. Landreman, “Neoclassical transport with non-trace impurities in density pedestals,” *Europhysics Conference Abstracts* **40A**, O4.118 (2016).
- ⁴⁶F. I. Parra and M. Barnes, “Intrinsic rotation in tokamaks: theory,” *Plasma Physics and Controlled Fusion* **57**, 045002 (2015).